JACS
JOURNAL OF THE AMERICAN CHEMICAL SOCIETY
Article
pubs.acs.org/JACS

Multiple Converged Conduction Bands in $K_2Bi_8Se_{13}$: A Promising Thermoelectric Material with Extremely Low Thermal Conductivity

Yanling Pei,[†] Cheng Chang,[†] Zhe Wang,[‡,∥] Meijie Yin,[‡,∥] Minghui Wu,[‡,∥] Gangjian Tan,[§] Haijun Wu,[‡,∥,⊥] Yuexing Chen,[‡,∥] Lei Zheng,[†] Shengkai Gong,[†] Tiejun Zhu,[#] Xinbing Zhao,[#] Li Huang,[‡,∥] Jiaqing He,[‡,∥] Mercouri G. Kanatzidis,*[,§] and Li-Dong Zhao*[,†]

[†]School of Materials Science and Engineering, Beihang University, Beijing 100191, China
[‡]Department of Physics, South University of Science and Technology of China, Shenzhen 518055, China
[§]Department of Chemistry, Northwestern University, Evanston, Illinois 60208, United States
[∥]Shenzhen Key Laboratory of Thermoelectric Materials, Shenzhen 518055, China
[⊥]Department of Materials Science and Engineering, National University of Singapore, 7 Engineering Drive 1, Singapore 117575, Singapore
[#]State Key Laboratory of Silicon Materials and School of Materials Science and Engineering, Zhejiang University, Hangzhou 310027, China

Supporting Information

ABSTRACT: We report that $K_2Bi_8Se_{13}$ exhibits multiple conduction bands that lie close in energy and can be activated through doping, leading to a highly enhanced Seebeck coefficient and a high power factor with elevated temperature. Meanwhile, the large unit cell, complex low symmetry crystal structure, and nondirectional bonding lead to the very low lattice thermal conductivity of $K_2Bi_8Se_{13}$, ranging between 0.42 and 0.20 W m^{-1} K^{-1} in the temperature interval 300−873 K. Experimentally, we further support the low thermal conductivity of $K_2Bi_8Se_{13}$ using phonon velocity measurements; the results show a low average phonon velocity (1605 ms^{-1}), small Young's modulus (37.1 GPa), large Grüneisen parameter (1.71), and low Debye temperature (154 K). A detailed investigation of the microstructure and defects was carried out using electron diffraction and transmission microscopy which reveal the presence of a $K_{2.5}Bi_{8.5}Se_{14}$ minor phase intergrown along the side of the $K_2Bi_8Se_{13}$ phase. The combination of enhanced power factor and low thermal conductivity results in a high ZT value of ∼1.3 at 873 K in electron doped $K_2Bi_8Se_{13}$ material.

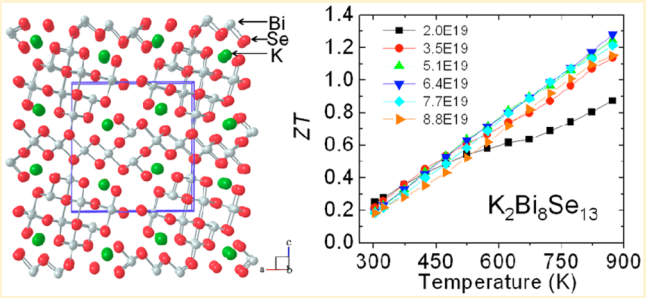

INTRODUCTION

Thermoelectric materials with high efficiencies are highly desired because they could directly converse thermal and electrical energy. The key parameter assessing the efficiency of thermoelectric materials is the "dimensionless figure of merit" ZT defined by $ZT = (S^2\sigma/\kappa)T$, where σ is the electrical conductivity, S is the Seebeck coefficient, κ is the total thermal conductivity (a sum of lattice thermal conductivity and electron thermal conductivity), and T is the temperature, respectively.[1,2] Ideally, high performance thermoelectric material should possess high electrical conductivity and Seebeck coefficient but minimum total thermal conductivity simultaneously. However, due to the well-known complicated relationship among the three parameters (S, σ, and κ), it is challenging to find effective approaches to improve an overall ZT, such as the Wiedemann−Franz law requiring κ_{ele} to be proportional to σ and the Pisarenko relation limiting the values of $S^2\sigma$ (power factor), which is the quantity that needs to be maximized.[3]

To date, the advanced approaches to increase ZT could be summarized as enhancing the power factor through tailoring of band structures,[4] reducing the thermal conductivity,[5] or both simultaneously.[6] Reducing lattice thermal conductivity (κ_{lat}) is an effective method to enhance ZT, since κ_{lat} is the only independent parameter.[7,8] The most effective approaches to reduce lattice thermal conductivity typically involve sophisticated design strategies, including atomic-, nano-, and mesoscale, and could be summarized as artistically named hierarchical architectures.[7] Apart from these, one can seek for low thermal conductivity in single phase compounds.[9,10] The low thermal conductivity may arise from an anharmonic and anisotropic bonding,[11,12] complex crystal structure,[13,14] very large unit cells,[15] large molecular weight,[16] atomic disorders induced by mobile ions,[17] lone-pair electrons,[12,18,19] rattling-like damping as a "resonant" phonon scattering,[20] etc.

Received: September 12, 2016
Published: November 28, 2016

DOI: 10.1021/jacs.6b09568
J. Am. Chem. Soc. 2016, 138, 16364−16371

Recently, the discovery of high performance in SnSe crystals has triggered intense research for similar systems.[10,11,21] The very high thermoelectric performance of the SnSe crystals over a broad temperature range originates from both the ultrahigh power factor due to multiple valence bands and the ultralow lattice thermal conductivities.[10,11,22] The $K_2Bi_8Se_{13}$ system described previously features complex crystal structure and low thermal conductivity.[23−28] However, no reports are available that describe the doping as well as the high temperature properties of this system. In this Article, we revisited $K_2Bi_8Se_{13}$ and investigated its electrical and thermal transport behaviors above room temperature. The thermal conductivity of polycrystalline samples of this material is ultralow and ranges from 0.42 to 0.20 W m^{-1} K^{-1} from 300 to 873 K, respectively. Meanwhile, the multiple conduction bands present in the electronic structure of $K_2Bi_8Se_{13}$, as indicated by density functional theory (DFT) calculations, point to an opportunity to enhance the power factor by populating these bands with electron carriers through doping. We show that pushing the Fermi level into the conduction band activates several Fermi electron pockets and produces enhanced Seebeck coefficients. This approach leads to both enhanced power factor and low thermal conductivity, resulting in a high ZT value of ~1.3 at 873 K.

RESULTS AND DISCUSSION

The experimental details are given in the Supporting Information, which include the starting materials, sample synthesis, the measurements for density, electrical, and thermal transport properties, transmission electron microscopy (TEM), X-ray diffraction, phonon velocity measurements, and density functional theory (DFT) computations.

1. Crystal Structure. As shown in Figure 1, $K_2Bi_8Se_{13}$ possesses a complex and anisotropic crystal structure. The

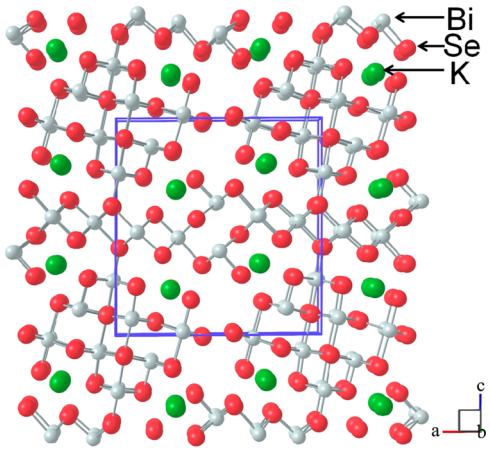

Figure 1. Crystal structure of $K_2Bi_8Se_{13}$.

$K_2Bi_8Se_{13}$ has a low-symmetry monoclinic structure that consists of two Bi/Se building blocks (NaCl type and Bi_2Se_3 type) connected at the K/Bi mixed site (green) to form a three-dimensional structure with narrow tunnels. The K atoms are located in these tunnels at the connection points between these building blocks, which are metal sites with special mixed occupancy of K/Bi. This indicates a highly anisotropic structure which grows along the b axis forming needlelike or columnar crystals. A closely related phase to $K_2Bi_8Se_{13}$ is $K_{2.5}Bi_{8.5}Se_{14}$ which often tends to grow as a minority phase.[23]

In this work, the $BiCl_3$ was chosen as a dopant to control the carrier concentration, since chlorides are electron dopants for selenides.[29,30] Figure 2a shows the powder XRD patterns of $K_2Bi_8Se_{13}$ samples with different levels of $BiCl_3$. All XRD peaks can be indexed to the simulated diffraction pattern of $K_2Bi_8Se_{13}$, with the exception of the weak peaks at around 20° 2θ which are indentified as the $K_{2.5}Bi_{8.5}Se_{14}$ phase. $K_{2.5}Bi_{8.5}Se_{14}$ is a different but structurally related phase to $K_2Bi_8Se_{13}$, and tends to form due to composition fluctuations in the synthesis reaction medium.[28] To obtain the relative amount of the $K_{2.5}Bi_{8.5}Se_{14}$ phase, Rietveld refinement was performed on the powder diffraction data using the software package Materials Analysis using Diffraction (MAUD)[31] with a satisfactory value of R_w = 3.18%. The weight fraction of $K_{2.5}Bi_{8.5}Se_{14}$ in the matrix-phase $K_2Bi_8Se_{13}$ is estimated at 28.68% (volume fraction 30.73%), as shown in Figure 2b. The refined lattice parameter for $K_2Bi_8Se_{13}$ is a = 1.72 nm, b = 0.42 nm, c = 1.83 nm, and α = 90.76°, while it is a = 1.78 nm, b = 0.47 nm, c = 2.18 nm, and α = 108.88° for $K_{2.5}Bi_{8.5}Se_{14}$.

2. Electronic Band Structure. Band structure and DOS calculations reveal that $K_2Bi_8Se_{13}$ is a semiconductor with a narrow band gap of 0.22 eV, consistent with that in previous studies;[27] see Figure 3a. Both the valence band maximum (VBM) and conduction band minimum (CBM) are located at the A point. Figure 3a clearly shows that the valence bands are multiple, and the energy gap between the valence bands located at the A point and Y point is less than 0.1 eV. However, the energy gaps of multiple conduction bands are so close; namely, the energy gap between the first and fourth bands is about 0.14 eV; this value is smaller than the 0.15 eV between the first and second valence bands of PbTe.[1,32] An orbital character analysis (Figure 3b−d) reveals that the VBM is mainly composed of Se-4p orbitals, while the CBM is dominated by hybridized Bi-6p and Se-4p states. In order to further understand electrical transport properties of $K_2Bi_8Se_{13}$, we have calculated the effective masses of VBM and CBM by eq 1. The effective masses were evaluated by fitting the dispersion relation around the VBM and CBM by a parabola

$$E_n(\vec{k}) = \frac{\hbar}{2m^*_{xx}}k_x^{\,2} + \frac{\hbar}{2m^*_{yy}}k_y^{\,2} + \frac{\hbar}{2m^*_{zz}}k_z^{\,2} \quad (1)$$

where $E_n(\vec{k})$ is the dispersion relation for the nth band, x, y, and z are directions in the reciprocal space, and m^*_{xx}, m^*_{yy}, and m^*_{zz} are the corresponding effective masses. In each direction around VBM and CBM, eigenvalues of seven sampling k-points with an interval of Δk = 0.003 au^{-1} were calculated for the fitting. We see that the calculated hole and electron effective masses are strongly anisotropic, with the smallest being along the b axis (parallel to the mixed K/Bi chains). As listed in Table 1, the average nondegeneracy DOS effective mass is ~0.44 m_0 for the first conduction band, obtained using the relationship, $m^* = (m_x^* m_y^* m_z)^{1/3}$.

3. Microstructure. To better explore the structure−property relationships of our $K_2Bi_8Se_{13}$ samples, we investigated the microstructural features using TEM techniques. A diversity of microstructural defects can be found in the $K_2Bi_8Se_{13}$ sample. The low magnification image shown in Figure 4a displays several grain boundaries with a size range from 100 nm to 3 μm. Within a typical grain, two phases appear to coexist, which are identified as $K_2Bi_8Se_{13}$ and $K_{2.5}Bi_{8.5}Se_{14}$; this observation is consistent with the XRD patterns presented above. The high magnification image of the grain in Figure 4b shows these two

DOI: 10.1021/jacs.6b09568
J. Am. Chem. Soc. 2016, 138, 16364−16371

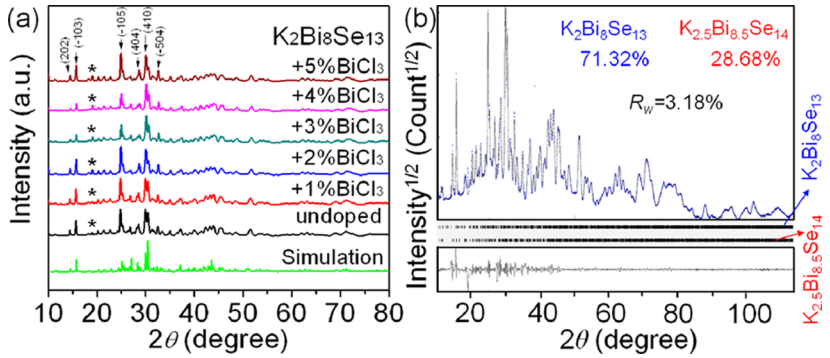

Figure 2. (a) X-ray diffraction pattern of $K_2Bi_8Se_{13}$ with different $BiCl_3$ doping fractions. The carrier concentrations are 2.0×10^{19}, 3.5×10^{19}, 5.1×10^{19}, 6.4×10^{19}, 7.7×10^{19}, and 8.8×10^{19} cm^{-3} for undoped, 1% $BiCl_3$, 2% $BiCl_3$, 3% $BiCl_3$, 4% $BiCl_3$, and 5% $BiCl_3$ doped $K_2Bi_8Se_{13}$, respectively. The extra peak labeled by a star is the $K_{2.5}Bi_{8.5}Se_{14}$ phase. (b) Rietveld refinement two-phase fitting of the diffraction data.

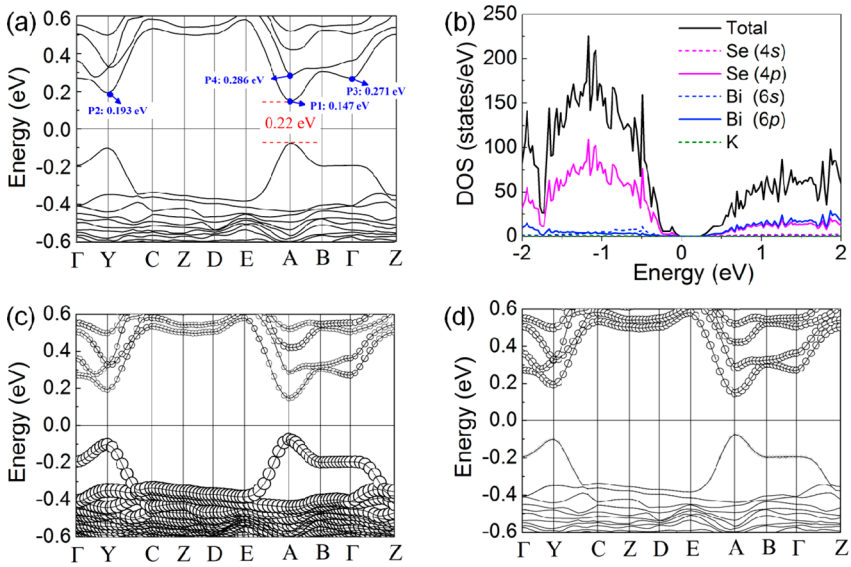

Figure 3. Electronic structure of $K_2Bi_8Se_{13}$ with spin−orbit coupling (SOC). (a) Band structure. (b) Total and projected density of states. (c and d) The p-orbital contributions (proportional to the circle size) of Se and Bi atoms, respectively.

Table 1. Calculated Effective Masses at Valence Band Maximum (VBM) and Conduction Band Minimum (CBM), Given in Units of the Free Electron Mass (m_e)

	VBM	CBM
m^*_{xx}/m_e	0.30	0.35
m^*_{yy}/m_e	0.15	0.19
m^*_{zz}/m_e	1.74	1.28

phases align in a parallel fashion. The (100) planes of the $K_2Bi_8Se_{13}$ phase (major) are parallel to the (100) planes of the $K_{2.5}Bi_{8.5}Se_{14}$ phase (minor), as observed along the selected area diffraction pattern observed down the [010] direction with an aperture observing both phases, Figure 4c. The images show that the two phases intergrow within a single grain instead of growing as individual grains. This results in plenty of two-phase boundaries at both the (100) side with a comparatively good lattice match (coherent) and the (001) side which has a great lattice mismatch. The concurrence of $K_2Bi_8Se_{13}$ and $K_{2.5}Bi_{8.5}Se_{14}$ phases could be due to comparable formation enthalpy at the present composition and process conditions as well as good lattice match along the (100) planes. It should be noted that such a large amount of coherent interfaces along the (001) planes could be beneficial for heat impedance. In addition, we observe that, even in a single phase domain of $K_2Bi_8Se_{13}$, a great amount of stacking faults (SF) are observed; see Figure 4d. One domain always has a 1/2 unit cell offset along the [100] direction relative to the adjacent one. All observed grains have a common crystal axis along the [010] direction which is the monoclinic *b*-axis.

Small angle grain boundaries (SAGB) with angles α less than 10° can often be found in the $K_2Bi_8Se_{13}$ sample. When viewed along [010] shown in Figure 4e, one can see that the orientations of the same phase at either side of the grain boundary are slightly rotated around the [010] axis by an angle α, which is also seen in the corresponding FFT pattern in Figure 4f.

4. Thermoelectric Transport Properties. In this work, the optimization strategy is based on the favorable electronic structure of the material, which can be described as below rational successive steps. In the beginning, we characterized the anisotropic features of the $K_2Bi_8Se_{13}$ samples with XRD characterization. Figure S1 shows XRD patterns of $K_2Bi_8Se_{13}$ bulk along the directions that are parallel and perpendicular to the spark plasma sintering (SPS) pressing direction. The patterns indicate a small anisotropy in crystallite orientation, which is consistent with the needle shape powders along the monoclinic *b*-axis of $K_2Bi_8Se_{13}$. The needle shape powders tend

DOI: 10.1021/jacs.6b09568
J. Am. Chem. Soc. 2016, 138, 16364−16371

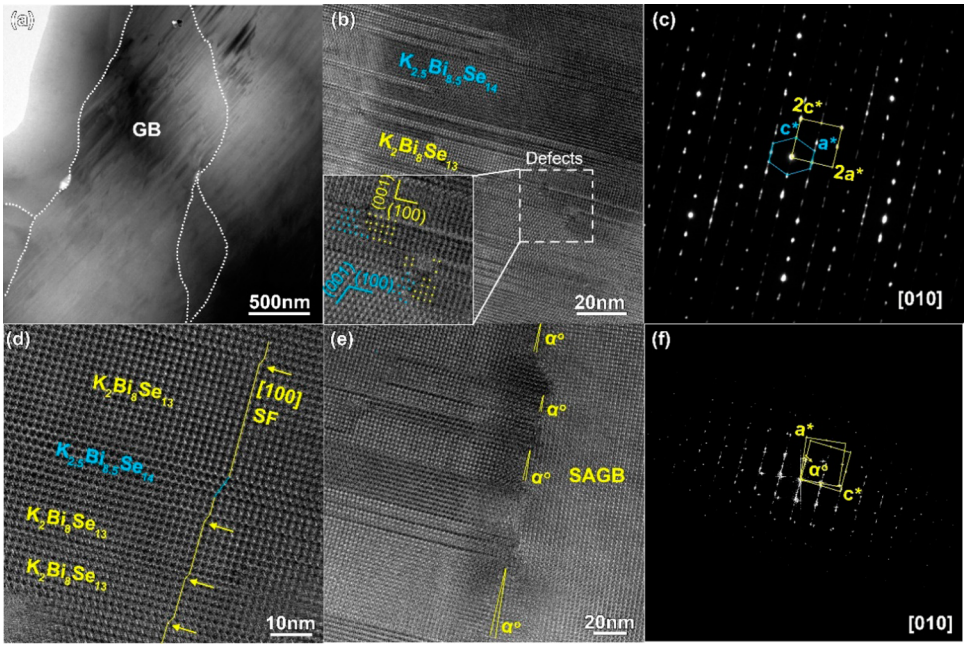

Figure 4. TEM images of the $K_2Bi_8Se_{13}$ along the [010] direction showing the following: (a) a general view at low magnification image, displaying a grain size of 100 nm to 3 μm; (b) a high magnification image showing $K_2Bi_8Se_{13}$ embedded with the $K_{2.5}Bi_{8.5}Se_{14}$ phase, (c) diffraction pattern of the binary phases ($K_2Bi_8Se_{13}$ and $K_{2.5}Bi_{8.5}Se_{14}$) indicated by two sets of indexes, (d) a great amount of stacking faults (SF) are observed in the $K_2Bi_8Se_{13}$ phase, both (e) small angle grain boundary (SAGB) and (f) diffraction pattern of the SAGB indicate a grain boundary angle of $\alpha < 10°$ in the $K_2Bi_8Se_{13}$.

to be perpendicular to the SPS direction. The anisotropic characters of $K_2Bi_8Se_{13}$ are well supported by the observed thermoelectric transport properties of $K_2Bi_8Se_{13}$ along two directions. It can be seen in Figure S2 that the electrical conductivity measured perpendicular to the pressing direction is superior to that parallel to the SPS direction and the Seebeck coefficients show almost isotropic behavior, resulting in a superior power factor along the perpendicular direction. However, the thermal conductivity is higher along the perpendicular direction, which can be compensated by the higher power factor. Finally, these results indicate that the *ZT* peak of ~0.9 at 873 K along the perpendicular direction is higher than the *ZT* value of ~0.7 along the parallel direction (Figures S2 and S3). Having determined the optimal sample direction for the thermoelectric properties, we then optimized these properties by using controlled amounts of $BiCl_3$ as dopant. In the next work, the thermoelectric properties of $K_2Bi_8Se_{13}$ were studied along the perpendicular direction.

Figure 5 shows the temperature dependence of thermoelectric properties for $K_2Bi_8Se_{13}$ samples with different carrier concentrations. With rising temperature, the electrical conductivity decreases from ~150 S cm^{-1} at 300 K to ~50 S cm^{-1} at 873 K for the sample with a carrier concentration of 2.0 × 10^{19} cm^{-3}, Figure 5a, which is derived from the Hall coefficient measurements (the Supporting Information shows the detailed measurements). The electrical conductivities increase significantly when the carrier concentration increases from 2.0 × 10^{19} to 8.8 × 10^{19} cm^{-3}. Specifically, with a carrier concentration of 8.8 × 10^{19} cm^{-3}, the electrical conductivity is ~450 S cm^{-1} (room temperature), almost 3 times larger than that of 2.0 × 10^{19} cm^{-3}. The rising carrier concentrations and electrical conductivities with increasing $BiCl_3$ fractions indicate that electron doping has been successful with $K_2Bi_8Se_{13}$.

Figure 5b shows that the Seebeck coefficient of undoped $K_2Bi_8Se_{13}$ is ~ −170 μV K^{-1} at 300 K and increases to ~ −270 μV K^{-1} at 873 K. Rising carrier concentrations result in the decline of the Seebeck coefficients, from ~ −170 μV K^{-1} for 2.0 × 10^{19} cm^{-3} to −100 μV K^{-1} for 8.8 × 10^{19} cm^{-3}.

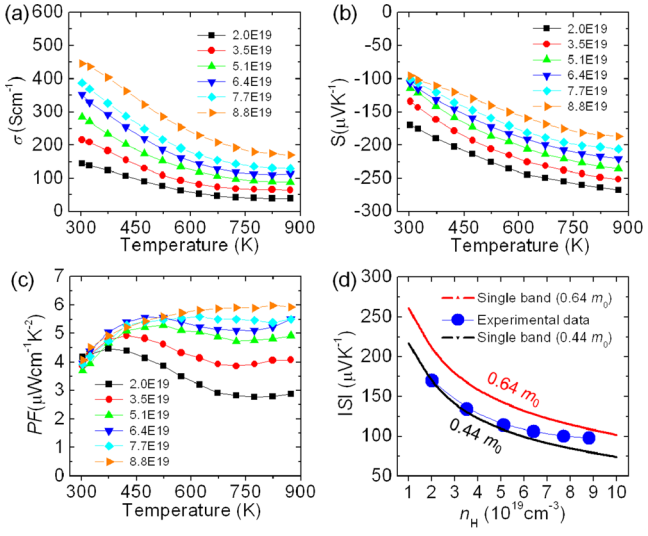

Figure 5. Thermoelectric properties as a function of temperature for $K_2Bi_8Se_{13}$ with different carrier concentrations: (a) electrical conductivity; (b) Seebeck coefficient; (c) power factor, and (d) Pisarenko plots at 300 K. The black solid line is the theoretical Pisarenko line that takes into account the first single conduction band with ~0.44 m_0, and the red solid line represents the theoretical Pisarenko line with ~0.64 m_0. The experimental Seebeck coefficient (blue spots) deviates to higher values with increasing carrier concentration, indicating multiple bands involved the electrical transports.

For the undoped sample, the power factor shows a maximum of ~4.5 μW cm^{-1} K^{-2} at room temperature and decreases to ~2.75 μW cm^{-1} K^{-2} at 773 K, as shown in Figure 5c. The

DOI: 10.1021/jacs.6b09568
J. Am. Chem. Soc. 2016, 138, 16364−16371

power factor peak shifts to higher temperature when the carrier concentration is increased, reaching ~6 μW cm^{-1} K^{-2} at 823 K with a carrier concentration of 8.8 × 10^{19} cm^{-3}, twice higher than that of the sample with 2.0 × 10^{19} cm^{-3}.

The power factor enhancements are ascribed to the high electrical conductivity while maintaining large Seebeck coefficients. If we compare the sample with a carrier concentration of 8.8 × 10^{19} cm^{-3} with samples of n-type lead chalcogenides and Bi_2Se_3 with similar carrier concentrations, the Seebeck coefficient of $K_2Bi_8Se_{13}$ is much larger. Namely, the Seebeck coefficient for $K_2Bi_8Se_{13}$ of ~ −105 μV K^{-1} is much higher than ~ −45 μV K^{-1} for PbTe,[33] ~ −40 μV K^{-1} for PbSe,[34] ~ −64 μV K^{-1} for PbS,[35] and ~ −80 μV K^{-1} for Bi_2Se_3[36] for a carrier concentration of ~6.0 × 10^{19} cm^{-3}. This is a strong enhancement and is related to the multiple conduction bands in the electronic structure that lie near each other in energy. As shown in Figure 3a, a small energy gap of 0.046 eV between first and second conduction bands can be observed and a gap of ~0.124 eV between first and third conduction bands can be observed. Because of these small energy gaps, several Fermi electron pockets can form simultaneously upon heavy n-type doping.[1,10,22,37,38] This expectation is well supported by the Pisarenko plot, which clearly shows the Seebeck coefficient enhancement, Figure 5d.

To further probe the origin of the Seebeck coefficient enhancements, we calculated this quantity using the non-parabolic single band Kane model.[32] In this model, carrier concentration is given by the formula

$$n = A^{-1}\frac{N_v(2m^*k_BT)^{3/2}}{3\pi^2\hbar^3}{}^0F_0^{3/2} \quad (2)$$

and Hall factor A

$$A = \frac{3K(K+2)}{(2K+1)^2}\frac{{}^0F_{-4}^{1/2}\cdot{}^0F_0^{3/2}}{({}^0F_{-2}^{1})^2} \quad (3)$$

and Seebeck coefficient

$$S = \frac{k_B}{e}\left[\frac{{}^1F_{-2}^{1}}{{}^0F_{-2}^{1}} - \eta\right] \quad (4)$$

${}^nF_k^m$ is a general form of the Fermi integral:[34]

$${}^0F_k^m = \int_0^\infty \left(-\frac{\partial f}{\partial \varepsilon}\right)\varepsilon^n(\varepsilon+\beta\varepsilon^2)^m[(1+2\beta\varepsilon)^2+2]^{k/2}\,d\varepsilon \quad (5)$$

In the above equations, k_B is the Boltzmann constant, $\hbar$ is the reduced Plank constant, ε is the reduced energy of the electron state, η is the reduced Fermi energy. N_v is the degeneracy of the CBM valley, which is 2 in our calculation. m^* is the nondegeneracy DOS effective mass, which is $(m_x^*m_y^*m_z)^{1/3}$, and K equals $m_z/(m_x^*m_y)^{1/2}$.

It can be clearly seen from Figure 5d that for high carrier concentrations (>5 × 10^{19} cm^{-3}) the experimentally observed Seebeck coefficients are higher than the values obtained by the single-band model using only the calculated DOS effective mass of the first conduction band ($m^* = 0.44m_0$), experimental Seebeck coefficients deviating to higher values with increasing carrier concentrations. In spite of a larger effective mass of $m^* = 0.64m_0$ (the Seebeck coefficient of the SPB model with $0.64m_0$ is comparable to the experimental data when the carrier concentration reaches 1 × 10^{20} cm^{-3}) being applied to match the experimental values, a significant difference still remains. To match the observed large Seebeck coefficients, a single-band model is therefore inadequate, suggesting the involvement of multiple bands in the electrical transport (i.e., the Fermi level is pushed up in energy with increasing carrier concentration, placing it into several conduction bands activating several Fermi pockets).

Figure 6a shows the total thermal conductivity as a function of temperature for $K_2Bi_8Se_{13}$ with different carrier concentrations. At room temperature, the κ_{tot} value of undoped $K_2Bi_8Se_{13}$ is about 0.5 W m^{-1} K^{-1}, which is extremely low in comparison with well-known thermoelectrics,[2,39,40] and continues to decrease with rising temperature, reaching a remarkably low value of ~0.30 W m^{-1} K^{-1} at 873 K. The total thermal conductivities increase with rising carrier concentrations because of the electronic thermal conductivity contributions. The lattice thermal conductivity (κ_{lat}) can be calculated through subtracting the electron part (κ_{ele}) from the total thermal conductivity (κ_{tot}) via the relationship $\kappa_{ele} = L\sigma T$, where L is the Lorenz number extracted on the basis of the approximately reduced chemical potential (η).[41,42] Figure S4 shows the thermal diffusivity, heat capacity, L number, and κ_{ele}, and the densities of samples are listed in Table S1. The lattice thermal conductivities show independent behaviors of doping level, and possess the very low value of ~0.20 W m^{-1} K^{-1} at 873 K, as shown in Figure 6b. One can see that the lattice thermal conductivity of $K_2Bi_8Se_{13}$ is comparable to these well-known materials with impressed low thermal conductivity,[11,15,43−46] Figure 6c. Specifically, the thermal conductivity of $K_2Bi_8Se_{13}$ is lower than those for BiCuSeO at 300−900 K.[43,47]

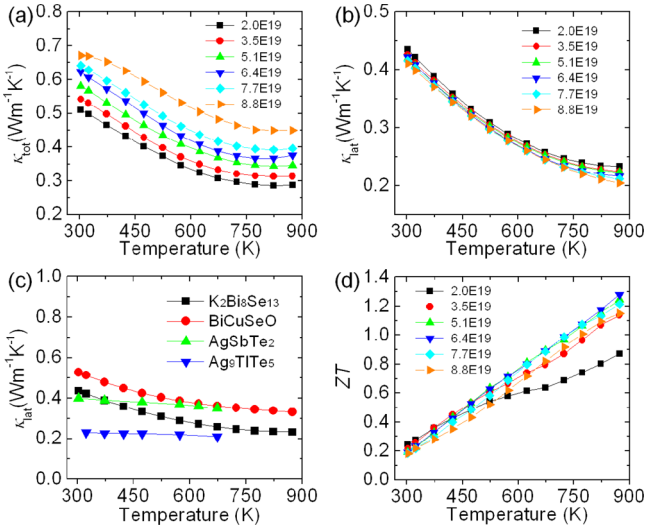

Figure 6. Thermoelectric properties as a function of temperature for $K_2Bi_8Se_{13}$ with different carrier concentrations: (a) total thermal conductivity; (b) lattice thermal conductivity; (c) lattice thermal conductivity comparisons of $K_2Bi_8Se_{13}$ and some typical thermoelectric with low thermal conductivity, and (d) ZT values.

The improved power factor and low thermal conductivity collectively contribute to the large ZT value. As shown in Figure 6d, a ZT value of ~1.3 at 873 K is reached for the sample with a carrier concentration of 6.4 × 10^{19} cm^{-3}. This demonstrates that $K_2Bi_8Se_{13}$ is a promising candidate for power generations.

DOI: 10.1021/jacs.6b09568
J. Am. Chem. Soc. 2016, 138, 16364−16371

5. Elastic Properties. The low thermal conductivity in $K_2Bi_8Se_{13}$ is remarkable. We believe that the microscale grain boundaries and nanoscale interfaces of $K_2Bi_8Se_{13}$ and possibly the minor $K_{2.5}Bi_{8.5}Se_{14}$ phase significantly scatter phonons with different wavelengths. To further elucidate the origin of the low thermal conductivity in the $K_2Bi_8Se_{13}$ system, we carried out the ultrasonic pulse echo measurements to evaluate the longitudinal (v_l) and shear (v_s) phonon velocities, Young's modulus (E), Grüneisen parameter (γ), and Debye temperature (θ_D). Generally, the small Young's modulus and large Grüneisen parameter reflect weak interatomic bonding strength and strong anharmonicity in the crystal lattice, respectively, both of which result in low lattice thermal conductivity via the formula as follows:[11,15,44,47−49]

$$\kappa = \frac{3.0 \times 10^{-5} \overline{M_a} a \theta_D^{\ 3}}{T \gamma^2 \nu^{2/3}} \tag{6}$$

$$\kappa \propto \frac{\rho^{1/6} E^{1/2}}{(M/m)^{2/3}} \tag{7}$$

where ρ is the sample density, $\overline{M_a}$ is the mean atomic weight of all the constituent atoms, a^3 is the average volume occupied by one atom, ν is the number of atoms in the unit primitive cell, M is the atomic weight of the molecule of the compound, and m is the number of atoms in the molecule. As shown above, eqs 6 and 7 summarize the key-variable interconnections quite nicely.

The average phonon velocity (v_a), Young's modulus (E), and Grüneisen parameter (γ) are given in the following relationships[15,47]

$$v_a = \left[\frac{1}{3}\left(\frac{1}{v_l^{\ 3}} + \frac{2}{v_s^{\ 3}}\right)\right]^{-1/3} \tag{8}$$

$$E = \frac{\rho v_s^{\ 2}(3v_l^{\ 2} - 4v_s^{\ 2})}{(v_l^{\ 2} - v_s^{\ 2})} \tag{9}$$

$$\gamma = \frac{3}{2}\left(\frac{1 + \upsilon_p}{2 - 3\upsilon_p}\right) \tag{10}$$

$$\upsilon_p = \frac{1 - 2(v_s/v_l)^2}{2 - 2(v_s/v_l)^2} \tag{11}$$

where ρ is the sample density, v_l is the longitudinal phonon velocity, v_s is the shear phonon velocity, and υ_p is the Poisson ratio, respectively. The phonon velocities were acquired directly by the ultrasonic pulse echo measurements, as listed in Table 2. The average phonon velocity (v_a), Young's modulus (E), and Grüneisen parameter (γ) for $K_2Bi_8Se_{13}$ are 1605 ms^{-1}, 37.1 GPa, and 1.77, respectively.

As shown in Table 2, the Young's modulus value of ~37.1 GPa for $K_2Bi_8Se_{13}$ is lower than these compounds,[43,44,47,50] such as ~70.3 GPa for Bi_2Se_3, ~76.5 GPa for BiCuSeO, and ~39.2 GPa for $AgSbTe_2$. The low Young's modulus is consistent with the low average phonon velocity arising from the weak chemical bonds, which is typically reflected by the elastic property comparisons between $K_2Bi_8Se_{13}$ and Bi_2Se_3. It is well-known that the lone pair electrons of Bi^{3+}, Sb^{3+}, and Sn^{2+} contribute significantly to the low thermal conductivity.[11,12,43,44,51] Here, the small Young's modulus and low thermal conductivity of $K_2Bi_8Se_{13}$ are believed to be partly derived from the lone pair of electrons in Bi^{3+}. As described in the report, the structure has several types of Bi atoms with greatly varying coordination environments. This gives low crystal symmetry and several types of distorted $BiSe_x$ (x = 5−8) polyhedra ranging from octahedra to singly capped or bicapped trigonal prisms. The Bi−Se bonds in the polyhedra vary significantly from 2.721 to 3.361 Å.[28] The distortions in the Bi coordination polyhedra are therefore large and reflect the strong tendency of the Bi^{3+} $6s^2$ lone electron pair to stereochemically express itself by occupying its own space. Only when the $BiSe_x$ coordination polyhedron is a perfect undistorted octahedron (x = 6) is the Bi^{3+} $6s^2$ lone pair of electrons completely quenched.[52] Therefore, the degree of distortion in each Bi polyhedron is a measure of the stereochemical expression. This implies a "soft" and highly anharmonic crystal lattice.

Table 2. Comparisons of Elastic Properties at Room Temperature of $K_2Bi_8Se_{13}$ and Other Materials with Low Thermal Conductivity

parameters	$K_2Bi_8Se_{13}$	Bi_2Se_3[50]	BiCuSeO[43,47]	$AgSbTe_2$[44]	Ag_9TlTe_5[15]
v_l (ms^{-1})	2683	3390	3290	3123	4420
v_s (ms^{-1})	1438	1870	1900	1538	1053
v_a (ms^{-1})	1605	2083	2107	1727	1203
E (GPa)	37.1	70.3	76.5	39.2	23.4
ν_p	0.30	0.28	0.25	0.34	0.47
γ	1.77	1.65	1.50	2.05	3.74
θ_D (K)	154	205	243	125	120

The lone pair of s electrons (from Bi^{3+} or Sb^{3+}) contributes to the Grüneisen parameters for $K_2Bi_8Se_{13}$, Bi_2Se_3, BiCuSeO, and $AgSbTe_2$ of 1.77, 1.65, 1.50, and 2.05, respectively.[43,44,47,50] Ag_9TlTe_5 possesses an extremely high Grüneisen parameter of ~3.74;[15] the very large Grüneisen parameter in Ag_9TlTe_5 is the result of the well-known anharmonic behavior of Ag atoms as well as the $6s^2$ lone pair of Tl.[53] The Ag_9TlTe_5 compound contains two different anharmonic ions each with a different mechanism of anharmonicity.

The value of Debye temperature also reflects the thermal conductivity to some extent; see eq 6. The Debye temperature θ_D is defined as follows[15]

$$\theta_D = \frac{h}{k_B}\left[\frac{3N}{4\pi V}\right]^{1/3} v_a \tag{12}$$

where h is Planck's constant, k_B is the Boltzmann constant, N is the number of atoms in a unit cell, V is the unit-cell volume, and v_a is the average phonon velocity, respectively. Using eq 12, we get that the Debye temperature of $K_2Bi_8Se_{13}$ is ~154 K, which is smaller than ~164 K for PbTe, ~190 K for PbSe, 205 K for Bi_2Se_3, and ~213 K for PbS,[15,40,50,54] consistent with the low thermal conductivity in the $K_2Bi_8Se_{13}$ system.

CONCLUDING REMARKS

The n-type $K_2Bi_8Se_{13}$ system is a promising thermoelectric material. Electron doping with $BiCl_3$ as dopant achieves carrier concentrations as high as 8.8×10^{19} cm^{-3} and high Seebeck coefficients. The enhanced Seebeck coefficients derive from populating the multiple conduction bands lying close in energy thanks to the special complex electronic structure of $K_2Bi_8Se_{13}$. Extremely low lattice thermal conductivities of 0.42−0.20 W m^{-1} K^{-1} were observed in the temperature ranges from 300 to 873 K. Direct phonon velocity measurements and elastic

DOI: 10.1021/jacs.6b09568
J. Am. Chem. Soc. 2016, 138, 16364−16371

properties suggest that the low thermal conductivities stem from the small Young's modulus, high Grüneisen parameter, and low Debye temperature, which are related to its complex low-symmetry monoclinic crystal structure. The combination of improved power factor and low thermal conductivity contributes to a high *ZT* of 1.3 at 873 K, which indicates that the $K_2Bi_8Se_{13}$ system is a potential thermoelectric material for power generation in the medium temperature range.

■ ASSOCIATED CONTENT

Supporting Information

The Supporting Information is available free of charge on the ACS Publications website at DOI: 10.1021/jacs.6b09568.

Experimental details; sample densities in the study (Table S1); XRD patterns of $K_2Bi_8Se_{13}$ bulks along directions parallel and perpendicular to the SPS pressing direction (Figure S1); thermoelectric properties for $K_2Bi_8Se_{13}$ along two directions (Figures S2 and S3); thermoelectric properties for $K_2Bi_8Se_{13}$ with different carrier concentrations (Figure S4); relaxed structure of $K_2Bi_8Se_{13}$ (Figure S5); the band gap of $K_2Bi_8Se_{13}$ (Figure S6); the thermogravimetric analysis (TGA) of $K_2Bi_8Se_{13}$ under N_2 flow (Figure S7) (PDF)

■ AUTHOR INFORMATION

Corresponding Authors

*m-kanatzidis@northwestern.edu
*zhaolidong@buaa.edu.cn

ORCID

Gangjian Tan: 0000-0002-9087-4048
Li-Dong Zhao: 0000-0003-1247-4345

Notes

The authors declare no competing financial interest.

■ ACKNOWLEDGMENTS

This work was supported by the Department of Energy, Office of Science Basic Energy Sciences, under grant DE-SC0014520 (M.G.K.). This work was also supported by the "Zhuoyue" program of Beihang University, the Recruitment Program for Young Professionals, NSFC under Grant No. 51571007, and the Fundamental Research Funds for the Central Universities (L.-D.Z., Y.P., C.C.) and 11404160 (L.H.). This work was also supported by the startup of South University of Science, Technology of China, the Recruitment Program for Young Professionals, the Science, Technology and Innovation Commission of Shenzhen Municipality (JCYJ 20140612140151884, KQCX2015033110182370, and JCYJ20150831142508365) (J.H.).

■ REFERENCES

(1) (a) Zhao, L.-D.; Dravid, V. P.; Kanatzidis, M. G. *Energy Environ. Sci.* **2014**, *7*, 251. (b) Tan, G. J.; Zhao, L.-D.; Kanatzidis, M. G. *Chem. Rev.* **2016**, *116*, 12123.

(2) Snyder, G. J.; Toberer, E. S. *Nat. Mater.* **2008**, *7*, 105.

(3) Zhu, T. J.; Fu, C. G.; Xie, H. H.; Liu, Y. T.; Zhao, X. B. *Adv. Energy Mater.* **2015**, *5*, 1500588.

(4) (a) Heremans, J. P.; Wiendlocha, B.; Chamoire, A. M. *Energy Environ. Sci.* **2012**, *5*, 5510. (b) Zhao, W. Y.; Wei, P.; Zhang, Q. J.; Peng, H.; Zhu, W. T.; Tang, D. G.; Yu, J.; Zhou, H. Y.; Liu, Z. Y.; Mu, X.; He, D. Q.; Li, J. C.; Wang, C. L.; Tang, X. F.; Yang, J. H. *Nat. Commun.* **2015**, *6*, 6197.

(5) (a) Poudel, B.; Hao, Q.; Ma, Y.; Lan, Y.; Minnich, A.; Yu, B.; Yan, X.; Wang, D.; Muto, A.; Vashaee, D. *Science* **2008**, *320*, 634. (b) Zhao, W. Y.; Wei, P.; Zhang, Q. J.; Dong, C. L.; Liu, L. S.; Tang, X. F. *J. Am. Chem. Soc.* **2009**, *131*, 3713.

(6) (a) Vineis, C. J.; Shakouri, A.; Majumdar, A.; Kanatzidis, M. G. *Adv. Mater.* **2010**, *22*, 3970. (b) Zhao, W. Y.; Liu, Z. Y.; Wei, P.; Zhang, Q. J.; Zhu, W. T.; Su, X. L.; Tang, X. F.; Yang, J. H.; Liu, Y.; Shi, J.; Chao, Y. M.; Lin, S. Q.; Pei, Y. Z. *Nat. Nanotechnol.* **2016**, DOI: 10.1038/nnano.2016.182.

(7) Biswas, K.; He, J. Q.; Blum, I. D.; Wu, C. I.; Hogan, T. P.; Seidman, D. N.; Dravid, V. P.; Kanatzidis, M. G. *Nature* **2012**, *489*, 414.

(8) Hsu, K. F.; Loo, S.; Guo, F.; Chen, W.; Dyck, J. S.; Uher, C.; Hogan, T.; Polychroniadis, E.; Kanatzidis, M. G. *Science* **2004**, *303*, 818.

(9) Zhang, X.; Zhao, L.-D. *J. Materiomics* **2015**, *1*, 92.

(10) Zhao, L. D.; Tan, G. J.; Hao, S. Q.; He, J. Q.; Pei, Y. L.; Chi, H.; Wang, H.; Gong, S. K.; Xu, H. B.; Dravid, V. P.; Uher, C.; Snyder, G. J.; Wolverton, C.; Kanatzidis, M. G. *Science* **2016**, *351*, 141.

(11) Zhao, L.-D.; Lo, S.-H.; Zhang, Y.; Sun, H.; Tan, G.; Uher, C.; Wolverton, C.; Dravid, V. P.; Kanatzidis, M. G. *Nature* **2014**, *508*, 373.

(12) Nielsen, M. D.; Ozolins, V.; Heremans, J. P. *Energy Environ. Sci.* **2013**, *6*, 570.

(13) Toberer, E. S.; May, A. F.; Snyder, G. J. *Chem. Mater.* **2010**, *22*, 624.

(14) Chung, D.-Y.; Hogan, T.; Brazis, P.; Rocci-Lane, M.; Kannewurf, C.; Bastea, M.; Uher, C.; Kanatzidis, M. G. *Science* **2000**, *287*, 1024.

(15) Kurosaki, K.; Kosuga, A.; Muta, H.; Uno, M.; Yamanaka, S. *Appl. Phys. Lett.* **2005**, *87*, 061919.

(16) Chung, D. Y.; Hogan, T. P.; Rocci-Lane, M.; Brazis, P.; Ireland, J. R.; Kannewurf, C. R.; Bastea, M.; Uher, C.; Kanatzidis, M. G. *J. Am. Chem. Soc.* **2004**, *126*, 6414.

(17) Liu, H.; Shi, X.; Xu, F.; Zhang, L.; Zhang, W.; Chen, L.; Li, Q.; Uher, C.; Day, T.; Snyder, G. J. *Nat. Mater.* **2012**, *11*, 422.

(18) Zhang, Y.; Skoug, E.; Cain, J.; Ozolins, V.; Morelli, D.; Wolverton, C. *Phys. Rev. B: Condens. Matter Mater. Phys.* **2012**, *85*, 054306.

(19) Lai, W.; Wang, Y.; Morelli, D. T.; Lu, X. *Adv. Funct. Mater.* **2015**, *25*, 3648.

(20) Qiu, W. J.; Xi, L. L.; Wei, P.; Ke, X. Z.; Yang, J. H.; Zhang, W. Q. *Proc. Natl. Acad. Sci. U. S. A.* **2014**, *111*, 15031.

(21) Li, C. W.; Hong, J.; May, A. F.; Bansal, D.; Chi, S.; Hong, T.; Ehlers, G.; Delaire, O. *Nat. Phys.* **2015**, *11*, 1063.

(22) Peng, K.; Lu, X.; Zhan, H.; Hui, S.; Tang, X.; Wang, G.; Dai, J.; Uher, C.; Wang, G.; Zhou, X. *Energy Environ. Sci.* **2016**, *9*, 454.

(23) Kyratsi, T.; Chung, D. Y.; Ireland, J. R.; Kannewurf, C. R.; Kanatzidis, M. G. *Chem. Mater.* **2003**, *15*, 3035.

(24) Kyratsi, T.; Hatzikraniotis, E.; Paraskevopoulos, K. M.; Malliakas, C. D.; Dyck, J. S.; Uher, C.; Kanatzidis, M. G. *J. Appl. Phys.* **2006**, *100*, 123704.

(25) Kyratsi, T.; Ioannou, M. *J. Electron. Mater.* **2013**, *42*, 1604.

(26) Bilc, D. I.; Mahanti, S. D.; Kyratsi, T.; Chung, D. Y.; Kanatzidis, M. G.; Larson, P. *Phys. Rev. B: Condens. Matter Mater. Phys.* **2005**, *71*, 085116.

(27) Hoang, K.; Tomic, A.; Mahanti, S. D.; Kyratsi, T.; Chung, D. Y.; Tessmer, S. H.; Kanatzidis, M. G. *Phys. Rev. B: Condens. Matter Mater. Phys.* **2009**, *80*, 125112.

(28) Chung, D.-Y.; Choi, K.-S.; Iordanidis, L.; Schindler, J. L.; Brazis, P. W.; Kannewurf, C. R.; Chen, B.; Hu, S.; Uher, C.; Kanatzidis, M. G. *Chem. Mater.* **1997**, *9*, 3060.

(29) Androulakis, J.; Chung, D. Y.; Su, X. L.; Zhang, L.; Uher, C.; Hasapis, T. C.; Hatzikraniotis, E.; Paraskevopoulos, K. M.; Kanatzidis, M. G. *Phys. Rev. B: Condens. Matter Mater. Phys.* **2011**, *84*, 155207.

(30) Wang, X.; Xu, J. T.; Liu, G. Q.; Fu, Y. J.; Liu, Z.; Tan, X. J.; Shao, H. Z.; Jiang, H. C.; Tan, T. Y.; Jiang, J. *Appl. Phys. Lett.* **2016**, *108*, 083902.

(31) Wu, H. J.; Chang, C.; Feng, D.; Xiao, Y.; Zhang, X.; Pei, Y. L.; Zheng, L.; Wu, D.; Gong, S. K.; Chen, Y.; He, J. Q.; Kanatzidis, M. G.; Zhao, L. D. *Energy Environ. Sci.* **2015**, *8*, 3298.

(32) Ravich, Y. I.; Efimova, B. A.; Smirnov, I. A. *Semiconducting Lead Chalcogenides*; Plenum Press: 1970; Vol. 5.
(33) LaLonde, A. D.; Pei, Y. Z.; Snyder, G. J. *Energy Environ. Sci.* **2011**, *4*, 2090.
(34) Wang, H.; Pei, Y. Z.; LaLonde, A. D.; Snyder, G. J. *Proc. Natl. Acad. Sci. U. S. A.* **2012**, *109*, 9705.
(35) Zhao, L. D.; Lo, S. H.; He, J.; Li, H.; Biswas, K.; Androulakis, J.; Wu, C. I.; Hogan, T. P.; Chung, D. Y.; Dravid, V. P.; Kanatzidis, M. G. *J. Am. Chem. Soc.* **2011**, *133*, 20476.
(36) Sk, R.; Shirolkar, M. M.; Dhara, B.; Kulkarni, S.; Deshpande, A. *Chem. Phys. Lett.* **2015**, *638*, 94.
(37) Pei, Y.; Shi, X.; LaLonde, A.; Wang, H.; Chen, L.; Snyder, G. J. *Nature* **2011**, *473*, 66.
(38) Pei, Y. Z.; Wang, H.; Snyder, G. J. *Adv. Mater.* **2012**, *24*, 6125.
(39) Kanatzidis, M. G. *Chem. Mater.* **2010**, *22*, 648.
(40) Goldsmid, H. *Conversion efficiency and figure-of-merit*, 1995.
(41) Zhao, L.-D.; He, J.; Wu, C.-I.; Hogan, T. P.; Zhou, X.; Uher, C.; Dravid, V. P.; Kanatzidis, M. G. *J. Am. Chem. Soc.* **2012**, *134*, 7902.
(42) Zhao, L.-D.; Lo, S.-H.; He, J.; Li, H.; Biswas, K.; Androulakis, J.; Wu, C.-I.; Hogan, T. P.; Chung, D.-Y.; Dravid, V. P.; Kanatzidis, M. G. *J. Am. Chem. Soc.* **2011**, *133*, 20476.
(43) Zhao, L.-D.; He, J.; Berardan, D.; Lin, Y.; Li, J.-F.; Nan, C.-W.; Dragoe, N. *Energy Environ. Sci.* **2014**, *7*, 2900.
(44) Morelli, D. T.; Jovovic, V.; Heremans, J. P. *Phys. Rev. Lett.* **2008**, *101*, 035901.
(45) Amouyal, Y. *Comput. Mater. Sci.* **2013**, *78*, 98.
(46) Wolfe, R.; Wernick, J. H.; Haszko, S. E. *J. Appl. Phys.* **1960**, *31*, 1959.
(47) Pei, Y. L.; He, J. Q.; Li, J. F.; Li, F.; Liu, Q. J.; Pan, W.; Barreteau, C.; Berardan, D.; Dragoe, N.; Zhao, L. D. *NPG Asia Mater.* **2013**, *5*, e47.
(48) Wan, C. L.; Pan, W.; Xu, Q.; Qin, Y. X.; Wang, J. D.; Qu, Z. X.; Fang, M. H. *Phys. Rev. B: Condens. Matter Mater. Phys.* **2006**, *74*, 144109.
(49) Berman, R. *Oxford studies in physics*, 1976.
(50) Gao, X.; Zhou, M.; Cheng, Y.; Ji, G. *Philos. Mag.* **2016**, *96*, 208.
(51) Skoug, E. J.; Morelli, D. T. *Phys. Rev. Lett.* **2011**, *107*, 235901.
(52) Zeier, W. G.; Zevalkink, A.; Gibbs, Z. M.; Hautier, G.; Kanatzidis, M. G.; Snyder, G. J. *Angew. Chem., Int. Ed.* **2016**, *55*, 6826.
(53) Lin, H.; Tan, G.; Shen, J.-N.; Hao, S.; Wu, L.-M.; Calta, N.; Malliakas, C.; Wang, S.; Uher, C.; Wolverton, C.; Kanatzidis, M. G. *Angew. Chem., Int. Ed.* **2016**, *55*, 11431.
(54) Veis, A.; Kaidanov, V.; Kuteinikov, R.; Nemov, S.; Rudenko, S.; Ukhanov, Y. I. *Soviet Physics Semiconductors-USSR* **1978**, *12*, 161.

DOI: 10.1021/jacs.6b09568
J. Am. Chem. Soc. 2016, 138, 16364−16371